UNIVERSITY OF BRISTOL

University of Bristol - Explore Bristol Research
General rights

Characterisation of slip and twin activity using digital image correlation and crystal plasticity finite element simulation: Application to orthorhombic α-uranium

Nicolò Grilli [a], Philip Earp [b], Alan C.F. Cocks [a], James Marrow [b], Edmund Tarleton [a,b,*]

[a] *Department of Engineering Science, University of Oxford, Parks Road, OX1 3PJ, UK*
[b] *Department of Materials, University of Oxford, Parks Road, OX1 3PH, UK*

ABSTRACT

Calibrating and verifying crystal plasticity material models is a significant challenge, particularly for materials with a number of potential slip and twin systems. Here we use digital image correlation on coarse-grained α-uranium during tensile testing in conjunction with crystal plasticity finite element simulations. This approach allows us to determine the critical resolved shear stress, interaction mechanisms and hardening rate of the different slip and twin systems. The constitutive model is based on dislocation densities and twin volume fractions as state variables, and the simulated geometry is constructed from electron backscatter diffraction images that provide shape, size and orientation of the grains, allowing a direct comparison between virtual and real experiments. An optimisation algorithm is used to discriminate between different models for the slip-twin interactions and to find the parameters that reproduce the evolution of the average strain in each grain as the load is increased. A tensile bar, containing four grains aligned with the load direction, is used to calibrate the model with eight unknown parameters. The approach is then independently validated by simulating the strain distribution in a second tensile bar. Different mechanisms for the hardening of the twin systems are evaluated, based on the interaction between coplanar and non-coplanar twins. The latent hardening of the most active twin system turns out to be determined by coplanar twins and slip. The hardening rate of the most active slip system is lower than in fine-grained α-uranium. The method outlined here can be applied to identify the critical resolved shear stress and slip-twin interaction mechanisms of other coarse-grained materials.

1. Introduction

Hardening in metals is due to interactions within, and between, the slip and twin systems (Kalidindi, 1998). The nucleation and motion of dislocations and twin nucleation and migration occur when the critical resolved shear stress (CRSS)

for these deformation mechanisms is reached (Devincre et al., 2008; Ojha et al., 2014). Since the seminal research of Asaro (1983), there has been significant effort dedicated towards the development of crystal based models for the inelastic deformation of engineering materials. Models of this type can contain a large number of material parameters, particularly if there are a number of different slip and twin systems that can be activated. A challenge then is to develop robust experimental procedures for the determination of these parameters. This either requires conducting a series of different experiments on polycrystalline materials covering a range of loading conditions and or stress states, or testing single crystals with different crystallographic configurations with respect to the loading direction (Franciosi et al., 1979). For a wide range of materials, particularly if they have limited ductility, each of these approaches might be impractical or even impossible to undertake. This is the case for the primary material of interest here - α-uranium (Inouye and Schaffhauser, 1969; Lander et al., 1994)

In this paper we demonstrate how the slip-twin interaction mechanisms and the material parameters can be determined from a single uniaxial test on a coarse grained material by comparing the detailed strain and displacement fields within the individual grains determined using digital image correlation (DIC) with crystal plasticity finite element (CPFE) simulations. For α-uranium, this makes it possible to discriminate between different constitutive models for the interaction between coplanar and non-coplanar twins, and to determine the 8 material parameters that describe the response of the different slip and twin systems that are active at room temperature. These parameters include the interaction strength between slip and twin systems. The approach can be readily generalised to other material systems.

Polycrystalline samples with columnar grains and arbitrary boundary conditions can be modelled using the crystal plasticity finite element (CPFE) method (Roters et al., 2018), which considers the anisotropic elastic behaviour, plastic deformation due to slip and twinning. Given the grain orientation, CPFE simulations provide the strain distribution in each grain (Dunne et al., 2007) and can be compared to digital image correlation (DIC) measurements (Lim et al., 2014).

The CPFE method has been widely used in conjunction with DIC measurements. For instance, DIC measurements can determine the local strain in polycrystalline samples, which is used for small scale CPFE simulations (Grilli et al., 2018; Nellessen et al., 2015). CPFE simulations are able to predict the strain localization (Irastorza-Landa et al., 2016) and lattice rotation (Irastorza-Landa et al., 2017b) in single crystals and oligocrystals, as detected by high resolution DIC (Guan et al., 2017). The DIC results can be correlated with the presence of geometrically necessary dislocations near grain boundaries (Roters et al., 2004). DIC has also been used to correlate strain concentrations with fracture paths (Khan and Marrow, 2009). As shown in the present study, the comparison between CPFE simulations and DIC measurements allows us to find the CRSS and hardening coefficients for the plastic deformation mechanisms in coarse-grained α-uranium.

In the CPFE method, the CRSS and hardening of the slip systems can be described by dislocation-based models, where the dislocation densities on the slip systems are the state variables (Grilli et al., 2015). An increase in dislocation density leads to hardening, usually described using a matrix detailing the strength of interactions between slip systems (Arsenlis and Parks, 2002). The dislocation density increase in α-uranium during deformation has not been systematically measured and few discrete dislocation dynamics studies appear in the literature (Behmer, 2018), which focus on the effect of twin thickness on dislocation pile-up and yield stress. The CRSS for slip and twinning have been identified for single crystal (Daniel et al., 1971) and fine-grained α-uranium (McCabe et al., 2010), obtained by hot or cold rolling. The interaction matrix between slip systems has been calibrated for fine-grained α-uranium (Knezevic et al., 2013a; McCabe et al., 2010) using polycrystal simulations and the visco-plastic self-consistent (VPSC) homogenization scheme (Hutchinson and Hill, 1970; Lebensohn and Tomé, 1993). This model has been used to simulate macroscopic α-uranium components (Knezevic et al., 2016) and has been validated over a broad range of strain rates and temperatures (Knezevic et al., 2013b). However, the CRSS and hardening have not been studied for coarse-grained α-uranium.

In the CPFE method, the interaction between twins and dislocations can be described using a CRSS for twin systems that depends on the accumulated shear on the slip systems (Abdolvand and Daymond, 2013a). The hardening rate of existing twins is also governed by the activity of coplanar and non-coplanar twins (Roters et al., 2010). This is based on the observation that, in FCC metals, deformation twinning initially produces only coplanar twins, while non-coplanar twin variants appear at larger strains (Kalidindi, 2001). As shown in this paper, the interaction between twins can be described using self hardening and latent hardening coefficients that couple the CRSS for twinning with the twin volume fraction on coplanar and non-coplanar twin systems. These interactions have not been included in previous constitutive models describing fine-grained α-uranium, calibrated using stress-strain curves (McCabe et al., 2010) and twin volume fraction measurements (Knezevic et al., 2012). However, polycrystal simulations and fine-grained samples, in which thousands of grains are considered and the twin volume fraction is low (Inouye and Schaffhauser, 1969), are not ideal to study twin-slip and twin-twin interactions. The same holds true for neutron diffraction experiments (Earp et al., 2018; Grilli et al., 2019, 2020), in which the measured lattice strain is averaged over a millimetre-sized gauge volume that contains many grains.

Coarse-grained α-uranium, obtained by casting, has a base centred orthorhombic crystal structure (Jacob and Warren, 1937; Kapoor et al., 2015; Lukesh, 1949) and grains reaching a size of several millimetres (Garlea et al., 2013). It is ideal to study slip-twin interactions because of the propensity to form several twins after quenching or deformation (Cahn, 1953; 1951). This is because the CRSS for twinning is comparable to the CRSS for slip. Plastic deformation mechanisms in α-uranium are strongly influenced by temperature (Daniel et al., 1971; Lloyd and Barrett, 1966), strain rate (Huddart et al., 1980), grain size (Inouye and Schaffhauser, 1969; Taplin, 1967), grain shape (Taplin and Martin, 1963), loading conditions (Zecevic et al., 2016a), hydrogen content (Calhoun et al., 2015) and alloying elements (Chen et al., 2017; Yanzhi et al., 2015). At room temperature, the most active slip system is the so-called "wall" slip system, which has the lowest CRSS up to

about 400 °C, followed by the "floor" slip system (Zecevic et al., 2016b). Other slip systems exist, such as the "chimney" slip system, with two variants, and the "roof" slip system, with four variants (Calhoun, 2016; Calhoun et al., 2018; 2013), but are observed only at high temperatures ($T > 873$ K) when the temperature is close to the $\alpha \rightarrow \beta$ phase transition (Daniel et al., 1971; Kapoor et al., 2015). The most commonly observed twin system is $\{130\}\langle 3\bar{1}0 \rangle$ (Brown et al., 2009), but a small fraction of '{172}'$\langle 3\bar{1}2 \rangle$ twins are also observed (Zhou et al., 2016). The '{176}'$\langle 512 \rangle$ twin system is observed only at high strain rate (Ho, 2012; Rollett et al., 1991).

As shown in the present study, tensile bars with a characteristic width of a few millimetres can be cut out from a larger polycrystalline plate made of coarse-grained α-uranium. The extruded area can be chosen such that only a small number of grains are present in the tensile bar aligned along the loading direction. High quality metallic surfaces, suitable for electron backscatter diffraction (EBSD) measurements, can be produced (Sutcliffe et al., 2018) and the grain orientation can be found. In-situ digital image correlation (DIC) measurements are carried out to measure the axial strain in each grain and the lateral displacement of the tensile bar. The stress-strain curve of each grain is subsequently obtained and compared with the simulated curves obtained with the CPFE method. A nonlinear optimisation procedure, based on the Nelder-Mead algorithm (Nelder and Mead, 1965), is used to find the CRSS and hardening rates of different slip systems. The optimisation procedures can validate the values of 4 parameters at a time against data from a tensile bar containing 4 grains. The Nelder-Mead optimisation technique has been used previously to fit stress-strain curves (Shen and Paulino, 2011), but this is the first application to tensile bars with columnar grains, in which the axial strain of individual grains is measured. Two tensile bars are used to validate the model by comparing the measured and simulated strain field. Different models for the hardening of the twin systems are compared (Kalidindi, 2001).

The hardening of the most active slip system ("wall" slip) in the coarse-grained material turns out to be lower than for fine-grained α-uranium (McCabe et al., 2010). It will be shown that the hardening of the most active twin system $\{130\}\langle 3\bar{1}0 \rangle$ due to coplanar twins and "floor" slip is able to explain the experimental results, and are therefore important mechanisms, which have not been previously identified. This is possible by choosing a grain in which one variant of this twin system has a Schmid factor greater than for the slip systems. The experimental technique and computational method developed in the present research can be applied to identify the CRSS and hardening parameters of other coarse grained materials.

In Section 2 the crystal plasticity model for slip and twinning is described. Section 2.2 contains the three different models for hardening of the twin systems which were tested. Experimental details are reported in Section 3. Section 4 contains the simulation results and the optimisation procedure to find the CRSS and hardening rates. The discussion and conclusions then follow in Sections 5 and 6 respectively.

2. Crystal plasticity finite element modelling

The crystal plasticity framework is based on the decomposition of the deformation gradient $\boldsymbol{F}$ into an elastic part $\boldsymbol{F}_e$, describing the stretch of the crystal lattice, and a plastic part $\boldsymbol{F}_p$, describing slip and twinning (Roters et al., 2012):

$$\boldsymbol{F} = \boldsymbol{F}_e \boldsymbol{F}_p . \tag{1}$$

The plastic deformation gradient $\boldsymbol{F}_p$ is an eigenstrain that does not contribute directly to the stress tensor. It has the following time evolution law (Kalidindi, 1998):

$$\boldsymbol{L}_p = \dot{\boldsymbol{F}}_p \boldsymbol{F}_p^{-1} = \left(1 - \sum_{\beta=1}^{N_{\text{twin}}} f_\beta \right) \sum_{\alpha=1}^{N_{\text{slip}}} \dot{\gamma}_\alpha (\boldsymbol{\sigma}) \boldsymbol{s}_\alpha \otimes \boldsymbol{n}_\alpha$$

$$+ \sum_{\beta=1}^{N_{\text{twin}}} \dot{f}_\beta (\boldsymbol{\sigma}) \gamma_\beta^{\text{twin}} \boldsymbol{s}_\beta \otimes \boldsymbol{n}_\beta . \tag{2}$$

The first term on the right hand side accounts for dislocation slip in the untwinned lattice, while the second term accounts for plastic deformation due to the creation of new twins. $\boldsymbol{L}_p$ is the plastic velocity gradient which relates $\boldsymbol{F}_p$ to its rate of change, $\dot{\boldsymbol{F}}_p$. $\dot{\gamma}_\alpha (\boldsymbol{\sigma})$ is the dislocation slip rate on slip system α; defined by the slip direction, $\boldsymbol{s}_\alpha$, and slip plane normal $\boldsymbol{n}_\alpha$. f_β is the twin volume fraction of twin system β (defined by the twin direction, $\boldsymbol{s}_\beta$, and twin plane normal $\boldsymbol{n}_\beta$) which increases at a rate of $\dot{f}_\beta (\boldsymbol{\sigma})$ whereas the shear produced by the twin system, $\gamma_\beta^{\text{twin}}$, is a constant. Note, that both $\dot{\gamma}_\alpha (\boldsymbol{\sigma})$ and $\dot{f}_\beta (\boldsymbol{\sigma})$ are stress dependent, as discussed in Section 2.1. The slip and twin systems used in the simulations are reported in Table 1.

The slip directions and slip plane normals are rotated from the lattice reference frame to the sample reference frame by a rotation matrix $\boldsymbol{R}$; which represents the grain orientation. $\boldsymbol{R}$ is updated at each time increment using the continuum elastic spin matrix, as explained in (Clausmeyer et al., 2011).

To model the nonlinear mechanical behaviour, at every time increment Δt of the simulation, the Cauchy stress increment $\Delta \boldsymbol{\sigma} = \boldsymbol{\sigma} - \boldsymbol{\sigma}_0$ is calculated as a function of the deformation gradient, where $\boldsymbol{\sigma}_0$ and $\boldsymbol{\sigma}$ are the Cauchy stress at the beginning and end of the time increment respectively. This is given by the anisotropic Hooke's law:

$$\Delta \boldsymbol{\sigma} = \mathbb{C} \Delta \boldsymbol{\varepsilon}_e + (\boldsymbol{W}_e \boldsymbol{\sigma}_0 - \boldsymbol{\sigma}_0 \boldsymbol{W}_e) \Delta t \tag{3}$$

where $\mathbb{C}$ is the fourth order elasticity tensor (Fisher and McSkimin, 1958) and $\boldsymbol{W}_e$ is the continuum elastic spin (Belytschko et al., 2014). The elastic constants for α-uranium are reported in Table 2. Details of the calculation of the

Table 1

Slip and twin systems used in the model (McCabe et al., 2010). The directions and plane normals are expressed in Cartesian coordinates and in the lattice coordinate system.

Slip system	s_α^0	n_α^0
$\alpha = 1$ (wall)	[1, 0, 0]	[0, 1, 0]
$\alpha = 2$ (floor)	[1, 0, 0]	[0, 0, 1]
$\alpha = 3$ (chimney)	[0.437, −0.899, 0]	[0.899, 0.437, 0]
$\alpha = 4$ (chimney)	[0.437, 0.899, 0]	[0.899, −0.437, 0]
$\alpha = 5$ (roof)	[0.241, −0.495, 0.835]	[0.0, 0.860, 0.510]
$\alpha = 6$ (roof)	[−0.241, −0.495, 0.835]	[0.0, 0.860, 0.510]
$\alpha = 7$ (roof)	[0.241, 0.495, 0.835]	[0.0, 0.860, −0.510]
$\alpha = 8$ (roof)	[0.241, −0.495, −0.835]	[0.0, 0.860, −0.510]
Twin system	s_β^0	n_β^0
$\beta = 1$	[0.825, −0.565, 0]	[0.565, 0.825, 0]
$\beta = 2$	[−0.825, −0.565, 0]	[−0.565, 0.825, 0]

Table 2

Elastic constants (GPa) at room temperature for the orthorhombic structure of α-uranium (Beeler et al., 2013; Fisher and McSkimin, 1958) in Voigt notation.

$\mathbb{C}_{11}$	$\mathbb{C}_{12}$	$\mathbb{C}_{13}$	$\mathbb{C}_{22}$	$\mathbb{C}_{23}$	$\mathbb{C}_{33}$	$\mathbb{C}_{44}$	$\mathbb{C}_{55}$	$\mathbb{C}_{66}$
214.74	46.49	21.77	198.57	107.91	267.11	124.44	73.42	74.33

elastic part of the small strain increment $\Delta \varepsilon_e$ are reported in Grilli et al., 2020. To find the stress increment that satisfies Eqs. (1), (2) and (3), an implicit equation for $\Delta \sigma$ is solved using a Newton–Raphson algorithm, as detailed in Dunne and Petrinic (2006); Dunne et al. (2007). The crystal plasticity framework is implemented in a user material subroutine (UMAT) for the finite element software Abaqus, which solves the equilibrium equation (Erinosho et al., 2013): $\nabla \cdot \sigma = 0$.

2.1. Constitutive model for slip and twinning

In this section the constitutive model to calculate the shear strain rate $\dot{\gamma}_\alpha(\sigma)$ for each slip system and the rate of increase of the twin volume fraction for each twin system is reported. A power law relationship is used for $\dot{\gamma}_\alpha(\sigma)$ (Asaro and Needleman, 1985):

$$\dot{\gamma}_\alpha(\sigma) = \dot{\gamma}_0 \left| \frac{\tau_\alpha}{\tau_\alpha^c} \right|^n \text{sign}(\tau_\alpha) \tag{4}$$

where $\dot{\gamma}_0$ and n are constants that determine the strain rate dependence and rate sensitivity of the slip activity. In the strain rate regime used in the present simulations and experiments, the model is weakly dependent on the choice of n. However, if the model is applied at high strain rate, further calibration of the plastic strain exponent n is required. τ_α is the resolved shear stress and τ_α^c is the CRSS of slip system α, which depends on the dislocation densities. Similarly, the rate of increase of the twin volume fraction depends on the resolved shear stress τ_β on the β twin system and is also assumed to follow a power law (Abdolvand and Daymond, 2013a):

$$\gamma_\beta^{\text{twin}} \dot{f}_\beta(\sigma) = \begin{cases} \dot{\gamma}_0 \left| \frac{\tau_\beta}{\tau_\beta^c} \right|^n & \text{if } \tau_\beta > 0 \\ 0 & \text{if } \tau_\beta < 0 . \end{cases} \tag{5}$$

The CRSS for twinning, τ_β^c, is weakly temperature dependent (Christian and Mahajan, 1995) and it can depend on dislocation density (Abdolvand and Daymond, 2013a). The present model is not able to resolve discrete twins, but only the average volume fraction can be studied. τ_β^c has to be interpreted as the stress necessary to nucleate individual twins (Remy, 1978). The stress necessary for twin propagation (Qiao et al., 2016) and migration (Ojha et al., 2014) is typically lower than this value. These softening mechanisms, leading to stress drops (Patriarca et al., 2013), are not included in the present model.

A twin system can be activated only by a positive resolved shear stress (Kalidindi, 1998). The CRSS for slip is linked to the evolution of dislocation densities (Beyerlein and Tomé, 2008; Madec et al., 2002; Mecking and Kocks, 1981):

$$\tau_\alpha^c = \tau_\alpha^0 + 0.9 \, b_\alpha \mu_\alpha \sqrt{\rho_\alpha^{\text{for}}} - 0.086 \, b_\alpha \mu_\alpha \sqrt{\rho^{\text{sub}}} \log \left(b_\alpha \sqrt{\rho^{\text{sub}}} \right) \tag{6}$$

where τ_α^0 is the initial slip resistance, b_α is the Burgers vector and μ_α is the projected shear modulus (Grilli et al., 2020) of the α slip system. ρ_α^{for} is the forest dislocation density, while ρ^{sub} represents dislocation debris that forms stable dislocation substructures at the onset of stage IV hardening (Beyerlein and Tomé, 2008; Madec et al., 2002). The logarithmic term in (6) represents the stress for gliding dislocations to bow out through arrays of locked dislocations with spacing $1/\sqrt{\rho^{\text{sub}}}$. This model was originally developed by Beyerlein and Tomé (2008) for pure Zr, who provide further details.

The hardening rate is determined by the time evolution of the dislocation densities (McCabe et al., 2010):

$$\dot{\rho}_\alpha^{\mathrm{for}} = k_\alpha^1 \frac{|\dot{\gamma}_\alpha(\boldsymbol{\sigma})|}{b_\alpha} \left[\sqrt{\rho_\alpha^{\mathrm{for}}} - \hat{d}_\alpha \rho_\alpha^{\mathrm{for}} \right] \tag{7}$$

$$\dot{\rho}^{\mathrm{sub}} = 1800 k_1^1 \hat{d}_1 \rho_1^{\mathrm{for}} \sqrt{\rho^{\mathrm{sub}}} |\dot{\gamma}_1(\boldsymbol{\sigma})| \tag{8}$$

where k_α^1 are dimensionless parameters and $\hat{d}_\alpha$ is the annihilation distance for slip system α.

The initial slip resistances τ_α^0 for $\alpha = 1, 2, 3$ ("wall", "floor", "chimney" slip systems) are three of the four parameters used in the optimisation procedure for the CRSS, described in Section 4.1, and the dimensionless parameters k_α^1 are three of the four parameters used in the optimisation procedure for the hardening.

The constitutive model for slip is local and does not include dislocation fluxes, therefore dislocations cannot propagate through the grain boundaries in the simulations.

2.2. Constitutive model for twin systems hardening

In the present study three hardening models for the twin systems are compared. The CRSS of the twin systems $(130)[3\bar{1}0]$ and $(\bar{1}30)[\bar{3}\bar{1}0]$ will be indicated by $\tau_{(130)}^c$ and $\tau_{(\bar{1}30)}^c$ in the following. The corresponding twin volume fractions will be indicated by $f_{(130)}$ and $f_{(\bar{1}30)}$. The first hardening model takes into account the interaction between twin and slip systems (Abdolvand and Daymond, 2013a). The CRSS for twinning is approximated with a linear function of the forest dislocation densities:

Twin-slip:
$$\tau_\beta^c = \tau_\beta^0 + k_\beta^1 \mu_\beta b_\beta \sum_{\alpha=1}^{N_{\mathrm{slip}}} b_\alpha \rho_\alpha^{\mathrm{for}} . \tag{9}$$

The second hardening model takes into account the interaction between the noncoplanar twin systems $(130)[3\bar{1}0]$ and $(\bar{1}30)[\bar{3}\bar{1}0]$. A constitutive description is proposed in which the CRSS for twinning is a linear function of the non-coplanar twin volume fraction:

Twin noncoplanar:
$$\tau_{(130)}^c = \tau_\beta^0 + k_\beta^1 \mu_\beta f_{(\bar{1}30)} \tag{10}$$

$$\tau_{(\bar{1}30)}^c = \tau_\beta^0 + k_\beta^1 \mu_\beta f_{(130)} . \tag{11}$$

The third hardening model also includes the interaction between coplanar twin systems:

Twin coplanar:
$$\tau_\beta^c = \tau_\beta^0 + k_\beta^1 \mu_\beta \left(f_{(130)} + f_{(\bar{1}30)} \right) . \tag{12}$$

τ_β^0 is the initial twin resistance, μ_β is the projected shear modulus (Grilli et al., 2020) on the twin system and k_β^1 is a dimensionless interaction parameter. τ_β^0 is the fourth parameter used in the optimisation procedure for the CRSS, described in Section 4.1. k_β^1 is the fourth parameter used in the optimisation procedure for the hardening. The three hardening models are referred to as the twin-slip, twin-noncoplanar and twin-coplanar model from here on. The complete set of model parameters are reported in Table 3.

3. Experimental details

Experiments were performed to measure the full-field surface strains during tensile deformation of cast α-uranium specimens with a known microstructure, using digital image correlation (DIC). Two dog-bone specimens were manufactured by AWE plc via wire electro-discharge machining (EDM) from a cast plate. The gauge dimensions were 32.00 mm $\times$ 6.00 mm, with a specimen thickness of 1.50 mm.

3.1. Sample preparation and EBSD

Sample preparation and EBSD microstructural characterisation were performed at the Interface Analysis Centre (IAC), School of Physics, University of Bristol, UK. Each specimen was mounted in Struers ClaroCit resin, and mechanically ground with 120 grit SiC paper to remove the oxide layer. Grinding with progressively finer papers, from 320 to 2500 grit, was followed by polishing with 6 μm and 3 μm diamond suspension. The specimens were removed from the resin with acetone, and electropolished at a voltage of 12 V in an electrolyte comprising a 10:6:6 volumetric ratio of ethanol, ethylene glycol, and phosphoric acid. The electrolyte was continuously stirred and polishing proceeded for between 10 and 20 min, until a smooth, reflective surface was observed.

EBSD analysis was performed on a Zeiss Sigma HD VP Field Emission SEM, with EDAX EBSD camera and associated OIM software. A series of large-area maps covering the whole gauge area were recorded with a slight overlap between each scan region. The EBSD datasets were post-processed using the MTEX toolbox (Bachmann et al., 2011) in MATLAB. The individual orientation maps were stitched together to produce a single map for the gauge region of each specimen.

Table 3
Model parameters.

Slip law parameters	Eq. (4)
Plastic strain rate coefficient ($\dot{\gamma}_0$)	0.001 s^{-1}
Plastic strain rate exponent (n) (Irastorza-Landa et al., 2017a)	20
Twin law parameters	**Eq. (5)**
Magnitude of shear due to twinning ($\gamma_\beta^{\text{twin}}$) (Cahn, 1953)	0.299
Initial twin volume fraction $f_\beta(t=0)$	0
Slip hardening law parameters	**Eq. (6)**
Constant friction stress (roof slip) ($\tau_5^0;\tau_6^0;\tau_7^0;\tau_8^0$) (Calhoun et al., 2013)	235 MPa
Burgers vector (wall slip) (b_1) (Lukesh, 1949)	0.285 nm
Burgers vector (floor slip) (b_2) (Lukesh, 1949)	0.285 nm
Burgers vector (chimney slip) ($b_3;b_4$) (Lukesh, 1949)	0.651 nm
Burgers vector (roof slip) ($b_5;b_6;b_7;b_8$) (Lukesh, 1949)	1.185 nm
Projected shear modulus (wall slip) (μ_1) (Fisher and McSkimin, 1958)	74.330 GPa
Projected shear modulus (floor slip) (μ_2) (Fisher and McSkimin, 1958)	73.420 GPa
Projected shear modulus (chimney slip) (μ_3, μ_4) (Fisher and McSkimin, 1958)	92.255 GPa
Projected shear modulus (roof slip) ($\mu_5, \mu_6, \mu_7, \mu_8$) (Fisher and McSkimin, 1958)	115.67 GPa
Dislocation density evolution law parameters	**Eqs. (7),(8)**
Dislocation multiplication prefactor (roof slip) ($k_5^1;k_6^1;k_7^1;k_8^1$) (McCabe et al., 2010)	0.948
Dislocation annihilation length (wall slip) ($\hat{d}_1$) (McCabe et al., 2010)	0.936 μm
Dislocation annihilation length (floor slip) ($\hat{d}_2$) (McCabe et al., 2010)	0.429 μm
Dislocation annihilation length (chimney slip) ($\hat{d}_3, \hat{d}_4$) (McCabe et al., 2010)	0.174 μm
Dislocation annihilation length (roof slip) ($\hat{d}_5, \hat{d}_6, \hat{d}_7, \hat{d}_8$) (McCabe et al., 2010)	0.124 μm
Initial dislocation density $\rho_\alpha^{\text{for}}(t=0) = \rho^{\text{sub}}(t=0)$	10^{10} m^{-2}
Twin hardening law parameters	**Eqs. (9)–(12)**
Twin Burgers vector (b_β)	0.1036 nm
Twin system projected shear modulus (μ_β)	99.537 GPa
Initial twin resistance (fitting parameter) τ_β^0	Table 4
Hardening coefficients (fitting parameters) k_β^1	Table 4
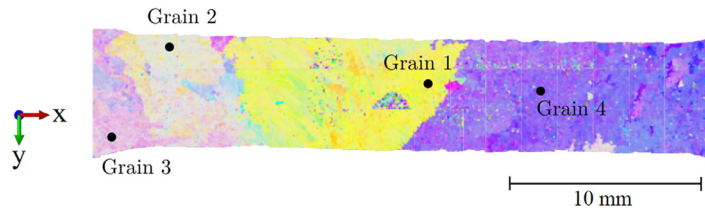
Fig. 1. EBSD orientation map of the first tensile bar. The black dots indicate the crystal orientations chosen for the four grains.
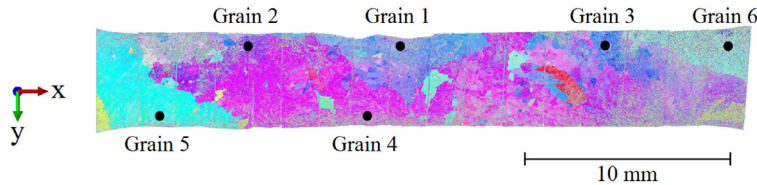
Fig. 2. EBSD orientation map of the second tensile bar. The black dots indicate the crystal orientations chosen for the six grains.

Figs. 1 and 2 show orientation maps from the two tensile bars, with colours representing the crystal direction parallel to the z direction (into-page). The microstructure is coarse, with sub-grains in excess of 200 μm in diameter clustered together into regions of similar orientations. Grain clusters are labelled according to their orientation; with 4 grains in the first tensile bar and 6 in the second.

3.2. In-situ mechanical testing

A speckle pattern of black and white acrylic paint was applied to the surface of each specimen with an airbrush. Tensile testing was performed on a Shimadzu Autograph AGS-X universal test machine with a 5 kN load cell, connected to a data acquisition PC running Shimadzu Trapezium-X software.
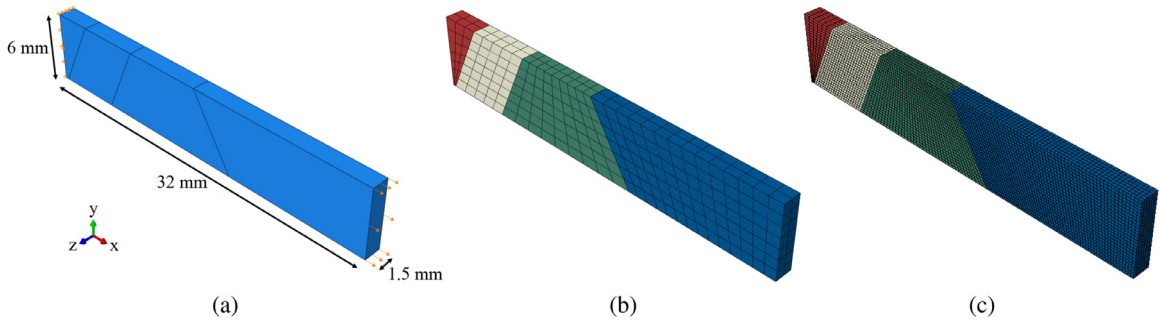
Fig. 3. (a) Representative volume of the first tensile bar. (b) Coarse mesh used during the optimisation procedure; different colours correspond to the Four different grains. (c) Fine mesh used for the validation procedure.
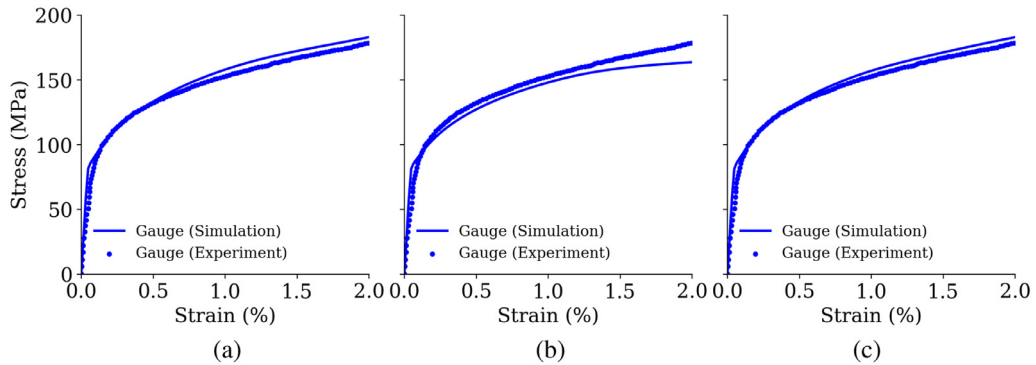
Fig. 4. Simulated and measured gauge stress-strain curves after the optimisation procedure using (a) the twin-slip model; equation (9), (b) the twin-noncoplanar model; Eqs. (10) and (11) and (c) twin-coplanar model; Eq. (12).

The specimen was enclosed in a bespoke sample holder to prevent contamination of the tensile grips. A window in the front face of the holder allows viewing of the specimen surface with the DIC cameras. The specimen was loaded in parallel with a thin ductile copper bar which would absorb energy in the event of specimen failure to prevent loss of radioactive material. The mechanical properties of the copper were characterised before the test; its flow curve was used to calculate the stress in the α-uranium specimen from the total load measured by the load cell. Each specimen was loaded in displacement control at a rate of either 0.05 mm/min or 0.025 mm/min.

DIC was performed with a GOM ARAMIS 5M stereo DIC system. The camera mounting frame was rotated by 90° from its usual horizontal orientation such that the affixed cameras were positioned above one another and angled inwards towards the specimen at an angle of 12.5°. This allowed the gauge section of the specimen to be viewed in a portrait orientation. A calibration process allowed the co-ordinates in each image to be related to 3D co-ordinates in a small calibrated volume centred on the specimen surface. Two camera DIC systems as used here allow the separation of in-plane strains from out-of-plane displacements, which cause strain artifacts in single-camera DIC. Illumination was provided by polarised light from high-intensity LEDs. A pair of DIC images was automatically acquired in the ARAMIS software every 2.5 seconds during the test.

The DIC analysis was performed with a facet size of 20 × 20 pixels and a 50% overlap between each facet. A rigid-body movement of the specimen before testing was used to calculate the in-plane strain error as ± 0.1%, and the error in out-of-plane displacement as ± 30 µm. The boundaries between the grain clusters in Fig. 1 were used to segment the DIC data such that the mean strain within each grain cluster can be calculated. This enables the plotting of stress-strain curves for the entire gauge volume (Fig. 4) and for the individual grain clusters (Fig. 5), for comparison with the simulation results. The stress used for these stress-strain curves (Fig. 5) is the one measured by the load cell and it is the same for all grain clusters because they are aligned with the load direction.

4. Simulation details and results

The representative volume used for the first tensile bar is shown in Fig. 3(a). The bar was 32 mm long and 6 mm wide. Displacement along the x axis was applied on the surface x = 32 mm. Zero displacement along the x direction was imposed on the surface x = 0. The point (x,y,z) = (0, 3, 0.75) mm was fixed to prevent translation of the surface x = 0. The points (x,y,z) = (0, 3, 1.5) mm and (x,y,z) = (0, 6, 0.75) mm can translate only along the z and y directions. This prevents rotation around the x axis of the surface x = 0. The texture of the representative volume consisted of four grains
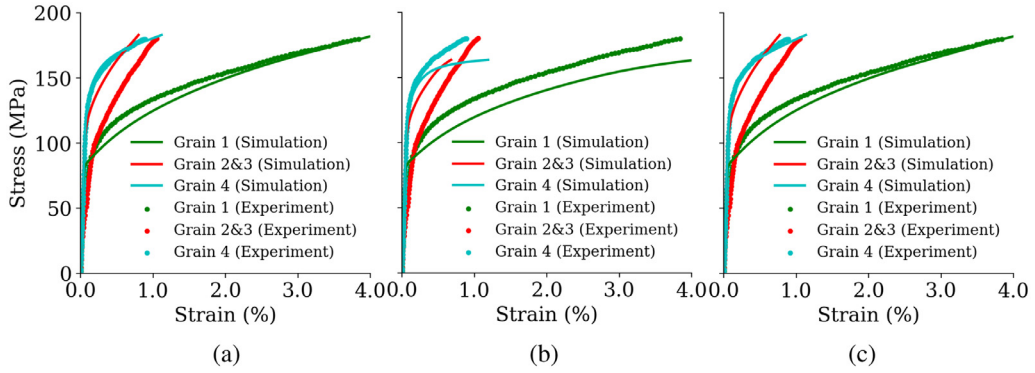
Fig. 5. Simulated and measured stress-strain curves in grain 1, grain 2&3 and grain 4 after the optimisation procedure using (a) the twin-slip model; equation (9), (b) the twin-noncoplanar model; Eqs. (10) and (11) and (c) twin-coplanar model; Eq. (12).

with different orientations (Fig. 3). This is a simplification compared to the experimental EBSD map (Fig. 1) but is useful to maintain constant Schmid factors in each grain and, therefore, to better understand the slip-twin activity in each grain. This approximation also avoids the introduction of spurious data at points where the experimental EBSD has larger uncertainty. An uncertainty quantification on the grain orientations has been carried out and its effect on the computational results is discussed in Section 5.

The coarser mesh used for the optimisation procedure is shown in Fig. 3(b). It consisted of 434 elements with an average size of around 1 mm. The coarser mesh is necessary to reduce the computational time during the optimisation procedure, which requires hundreds of simulations. A finer mesh, of 19,500 elements, shown in Fig. 3(c), was used to repeat the simulation with the optimised parameters and compare the simulated and experimental strain fields.

The maximum time increment used in the simulations was 0.04 s and the total time was 20 s, after which a total strain of 2% was reached. Therefore, the simulated strain rate was 10^{-3} s^{-1}: this value corresponds to the constant $\dot{\gamma}_0$ in Eq. (4) and was chosen to simulate the regime in which the model is strain rate independent (Capolungo et al., 2009). In this regime, the resolved shear stress on a slip or twin system remains close to the CRSS τ_α^c or τ_β^c respectively. At the beginning of the simulations, the twin volume fractions were set to zero and the dislocation densities were set to 10^{10} m^{-2}.

4.1. Optimisation procedure

The first optimisation procedure was carried out to find the initial CRSS parameters τ_α^0 and τ_β^0 for "wall" slip ($\alpha = 1$), "floor" slip ($\alpha = 2$), "chimney" slip ($\alpha = 3$) and the $\{130\}\langle 3\bar{1}0\rangle$ twin ($\beta = 1$). A nonlinear optimisation procedure, based on the Nelder–Mead algorithm (Nelder and Mead, 1965), was used, which is implemented in the `scipy.optimize` package (Jones et al., 2001). This algorithm was used because it does not require an analytical expression for the Jacobian. At every iteration of the algorithm, the simulation with the coarse mesh in Fig. 3 (b) was run with a set of parameters τ_α^0, τ_β^0. For each grain in Fig. 1 the axial strain was averaged; denoted $\bar{\varepsilon}^{G1}$, $\bar{\varepsilon}^{G2\&3}$ and $\bar{\varepsilon}^{G4}$, for grains 1, 2 and 3, 4 respectively. The strain was averaged together in grains 2 and 3 because their mechanical behaviour was similar. The total strain in the tensile bar is referred to as $\bar{\varepsilon}^{gauge}$ and the stress was averaged over the load surface in Fig. 3(a). This post-processing allows stress-strain curves to be extracted from the tensile bar and from the individual grains. The yield stresses of the tensile bar, σ_y^{gauge}, and of the individual grains, σ_y^{G1}, $\sigma_y^{G2\&3}$, σ_y^{G4}, were defined using the 0.1% offset criterion (Pham et al., 2013) for both the experiment and the simulation. It is possible to apply this offset criterion both for the global and averaged strain in individual grains because the grain clusters are millimetres in size, and so behave microscopically. The residual minimised by the Nelder–Mead algorithm was:

$$R_{CRSS} = \left(\sigma_{y,exp}^{gauge} - \sigma_{y,sim}^{gauge}\right)^2 + \left(\sigma_{y,exp}^{G1} - \sigma_{y,sim}^{G1}\right)^2 + \left(\sigma_{y,exp}^{G2\&3} - \sigma_{y,sim}^{G2\&3}\right)^2 + \left(\sigma_{y,exp}^{G4} - \sigma_{y,sim}^{G4}\right)^2 \quad (13)$$

where the subscripts exp and sim indicate experimental and simulated quantities. After every iteration of the Nelder–Mead algorithm, the parameters τ_α^0 and τ_β^0 are updated. This first optimisation procedure is carried out without considering the hardening of the twin systems because this does not significantly affect the yield stress. The CRSS parameters τ_α^0 and τ_β^0 that minimise the residual R_{CRSS} in Eq. (13) are given in Table 4.

A second optimisation procedure was then carried out to find the hardening parameters k_α^1 and k_β^1 for "wall" slip ($\alpha = 1$), "floor" slip ($\alpha = 2$), "chimney" slip ($\alpha = 3$) and the $\{130\}\langle 3\bar{1}0\rangle$ twin ($\beta = 1$) using the CRSS parameters τ_α^0 and τ_β^0 obtained from the first optimisation procedure. The hardening parameters k_α^1 and k_β^1 were updated after every iteration of the Nelder–Mead optimisation algorithm, in which a simulation with the coarse mesh in Fig. 3(b) up to 2% total strain was run. The maximum stress of the tensile bar reached during the deformation is denoted σ^{gauge}. The maximum total axial strain in

Table 4
Parameters obtained from the optimisation procedures for the CRSS and for the hardening rate. The three values of the parameters k_1^1, k_2^1, k_3^1, k_4^1 and k_β^1 are obtained using the twin-slip, twin-noncoplanar and twin-coplanar model respectively.

CRSS parameters optimisation	Eq. (6) and (9)–(12)		
Constant friction stress (wall slip) (τ_1^0)	24.5 MPa		
Constant friction stress (floor slip) (τ_2^0)	85.5 MPa		
Constant friction stress (chimney slip) ($\tau_3^0;\tau_4^0$)	166.5 MPa		
Twin resistance ({130} twin system) (τ_β^0)	55.5 MPa		
Hardening parameters optimisation	Eq. (9)	(10)-(11)	(12)
Dislocation multiplication prefactor (wall slip) (k_1^1)	0.0121	0.0088	0.0123
Dislocation multiplication prefactor (floor slip) (k_2^1)	0.36	1.69	1.80
Dislocation multiplication prefactor (chimney slip) ($k_3^1;k_4^1$)	0.136	0.176	0.0
Twin system hardening parameter (k_β^1)	4706	0.0570	0.00097
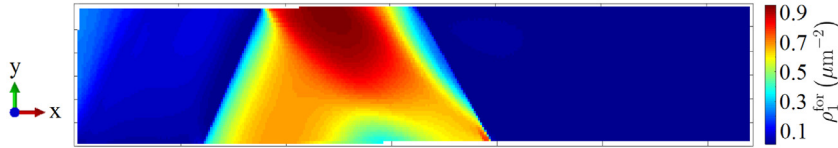
Fig. 6. Dislocation density ρ_1^{for} in the wall slip system in the first tensile bar at 1% total strain using the twin-coplanar model of equation (12).

the tensile bar is denoted $\bar{\varepsilon}^{\text{gauge}}$, and the maximum average axial strains reached during the deformation in the individual grains, $\bar{\varepsilon}^{\text{G1}}$, $\bar{\varepsilon}^{\text{G2&3}}$, $\bar{\varepsilon}^{\text{G4}}$, were calculated after each simulation. The residual minimised during the second optimisation procedure:

$$R_{\text{hard}} = R_{\text{hard}}^\sigma + \left(10^4 \text{ MPa}\right)^2 R_{\text{hard}}^{\bar{\varepsilon}} \tag{14}$$

where

$$R_{\text{hard}}^\sigma = 4\left(\sigma_{\text{exp}}^{\text{gauge}} - \sigma_{\text{sim}}^{\text{gauge}}\right)^2 \tag{15}$$

and

$$R_{\text{hard}}^{\bar{\varepsilon}} = \left(\bar{\varepsilon}_{\text{exp}}^{\text{gauge}} - \bar{\varepsilon}_{\text{sim}}^{\text{gauge}}\right)^2 + \left(\bar{\varepsilon}_{\text{exp}}^{\text{G1}} - \bar{\varepsilon}_{\text{sim}}^{\text{G1}}\right)^2 + \left(\bar{\varepsilon}_{\text{exp}}^{\text{G2&3}} - \bar{\varepsilon}_{\text{sim}}^{\text{G2&3}}\right)^2 + \left(\bar{\varepsilon}_{\text{exp}}^{\text{G4}} - \bar{\varepsilon}_{\text{sim}}^{\text{G4}}\right)^2 \tag{16}$$

was determined for the three different hardening models for the twin systems reported in Section 2.2. The hardening parameters k_α^1 and k_β^1 that minimise the residual R_{hard} in (14) are reported in Table 4.

The simulated stress-strain curves obtained using the optimised parameters and the three different hardening models for the twin systems are shown in Fig. 4 alongside the experimental data.

Fig. 5 shows stress as a function of the average axial strains $\bar{\varepsilon}^{\text{G1}}$, $\bar{\varepsilon}^{\text{G2&3}}$, $\bar{\varepsilon}^{\text{G4}}$ in the individual grains for the three different hardening models for the twin systems. The stress-strain curves agree with the experiment for the twin-slip (Fig. 5(a)) and for the twin-coplanar (Fig. 5(c)) interaction models. In grains 2 and 3, the maximum stress agrees with the experiment, as shown in Fig. 5(a) and (c), while the maximum strain is underestimated by the models.

The twin-noncoplanar interaction model is not able to match the stress value reached in the experiment, as shown in Figs. 4(b) and 5(b). It overestimates the strain accommodated in grain 4, as shown in Fig. 5(b). This will be interpreted in the following section according to the activity of the slip and twin systems.

4.2. Fine mesh simulation results and model validation

Once the optimal parameters τ_α^0, τ_β^0, k_α^1, k_β^1 were found, the simulation of the first tensile bar was repeated using the finer mesh in Fig. 3(c). The model chosen for the hardening of the twin systems was the twin-coplanar model described by Eq. (12) as this provides the best optimised fit to the experimental data. The "wall" slip system was the most active because of the lower CRSS, as reported in Table 4. Fig. 6 shows the dislocation density ρ_1^{for} in the "wall" slip system at 1% total strain. "Wall" slip is mostly active in grain 1 and the dislocation density grows by a factor of approximately 100 compared with the initial value.

Fig. 7 shows the twin volume fraction f_β at 2% total strain. It grows in the upper part of grain 4 and at the interface between grain 1 and grain 4, reaching a value of about 12%. We have found that the contribution to the twin volume fraction of the system $(130)[\bar{3}10]$ is much larger than the contribution of $(\bar{1}30)[\bar{3}\bar{1}0]$. The twin-slip model and the twin-coplanar model lead to the correct prediction of the stress-strain curve in grain 4, as shown in Fig. 5(a) and (c). The optimisation procedure allows us to find the interaction coefficients between coplanar twins and between slip and twin systems.
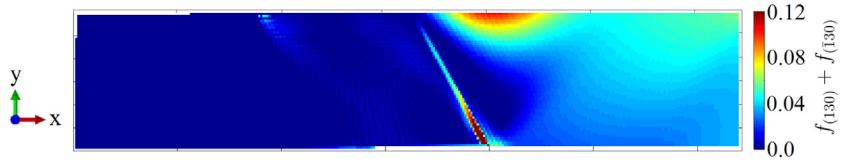
Fig. 7. {130} Twin volume fraction in the first tensile bar at 2% total strain for the twin-coplanar model of equation (12).
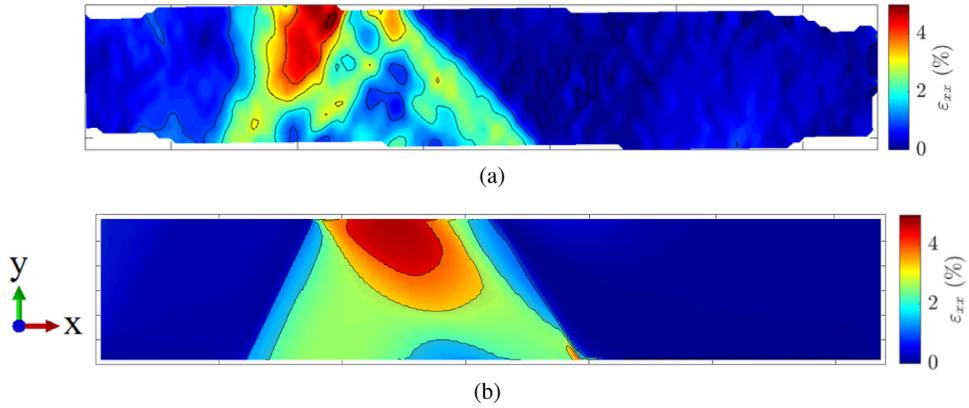

Fig. 8. Axial strain ε_{xx} in the first tensile bar at 1% total strain: (a) DIC measurement, (b) simulation.
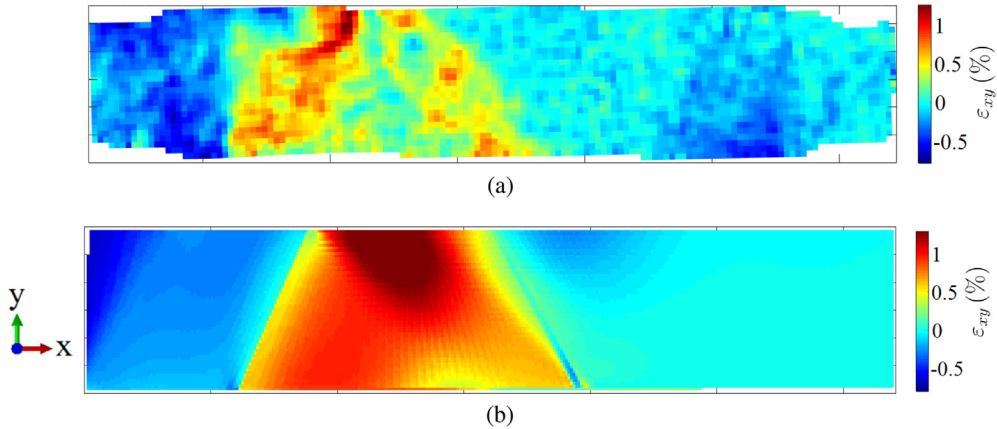

Fig. 9. Shear strain ε_{xy} in the first tensile bar at 1% total strain: (a) DIC measurement, (b) simulation.

The detailed strain and displacement fields within the grains provide additional information that can be used to validate the model resulting from the optimisation procedure. The axial strain concentrates in the upper part of grain 1 due to the activity of the "wall" slip system, as shown in Fig. 8. This agrees with the DIC measurement. The same slip activity leads to the concentration of the shear strain component ε_{xy} in the upper part of grain 1, as shown in Fig. 9.

The measured and predicted out-of-plane displacement u_z is shown as a surface plot in Fig. 10. The simulation results can be interpreted by studying the direction of the Burgers vectors of the "wall" slip system and of the {130} twin system. The largest component of these vectors is the u_z component, which is positive. This is found by multiplying the rotation matrices $\boldsymbol{R}$ of grains 1 and 4 and the slip and twin directions $\boldsymbol{s}^0_{\alpha=1}$ and $\boldsymbol{s}^0_{\beta=1}$ in the lattice reference system. Therefore, the large activity of the "wall" slip system in the upper part of grain 1 leads to positive u_z in that region. The same can be stated for the large twin activity on the bottom part of the grain boundary between grain 1 and 4, shown in Fig. 7. This agrees with the DIC measurement in Fig. 10(a).

The twin-noncoplanar model described by Eqs. (10) and (11) does not predict strong hardening of the most active twin system $(130)[3\bar{1}0]$ in grain 4. This explains the underestimation of the maximum stress reached in grain 4 using the twin-noncoplanar model, as shown in Fig. 5(b).
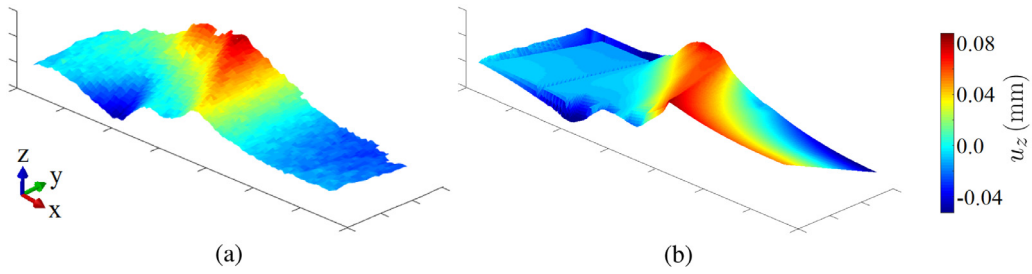
Fig. 10. Out-of-plane displacement u_z in the first tensile bar at 1% total strain: (a) DIC measurement, (b) simulation.

Table 5
Bunge–Euler angles in degrees. The corresponding rotation matrix, representing an active rotation, is a composition of intrinsic rotations about the axes z-x'-z".

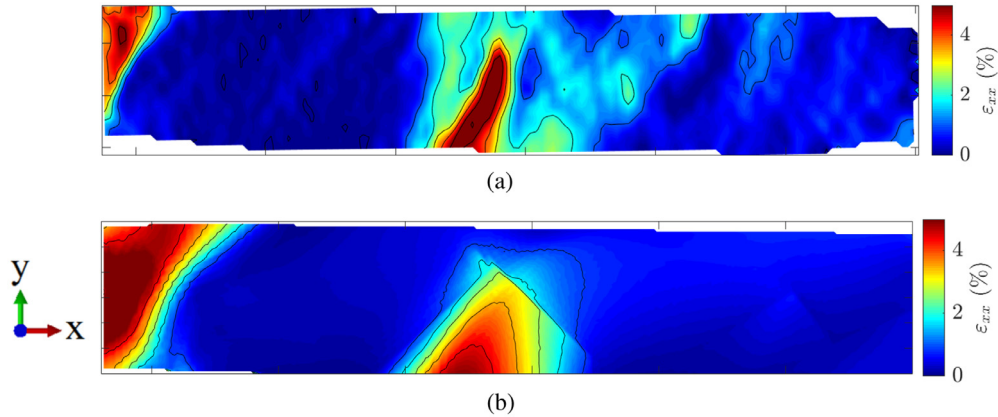| First tensile bar	Grain 1	Grain 2	Grain 3	Grain 4		
ϕ_1	219°	161°	329°	149°		
Φ	50°	116°	71°	101°		
ϕ_2	104°	67°	303°	159°		
Second tensile bar	Grain 1	Grain 2	Grain 3	Grain 4	Grain 5	Grain 6
ϕ_1	154°	124°	150°	128°	30°	321°
Φ	101°	85°	104°	87°	131°	137°
ϕ_2	49°	17°	4°	40°	176°	159°

Fig. 11. Axial strain ε_{xx} in the second tensile bar at 1% total strain: (a) DIC measurement, (b) simulation.

An independent model validation was obtained by simulating the second tensile bar with 6 grains shown in Fig. 2 (grain orientations for both bars are in Table 5). A fine mesh with 15,984 elements was used. The boundary conditions were the same as for the first tensile bar, shown in Fig. 3(a). The same model parameters τ_α^0, τ_β^0, k_α^1, k_β^1, optimised for the first tensile bar, were used. The model chosen for the hardening of the twin systems was again the twin-coplanar model described by Eq. (12). The measured and predicted axial strains are shown in Fig. 11. The "wall" slip system is active in grains 1 and 5, leading to strain concentration in those grains. The same slip activity leads to the concentration of the shear strain component ε_{xy} in grain 1 and 5, as shown in Fig. 12.

The measured and predicted out-of-plane displacement u_z is shown in Fig. 13. A rotation of about 1° around the x axis is added to the simulation results to match the experimental inclination on the surface $x = 0$, which was not present in the first tensile bar. Both the measurement and the simulation show a negative region of u_z corresponding to grain 1.

5. Discussion

The optimisation method presented in Section 4.1 shows that it is possible to use a single tensile bar experiment and DIC measurements to calibrate the yield strength and hardening rate of a crystal plasticity constitutive model for α-uranium. This material has slip and twin systems with very different properties. The reliability of the method is confirmed by the correct prediction of the strain and displacement fields, as shown in Figs. 8–13. This optimisation technique can be readily adapted to other materials.
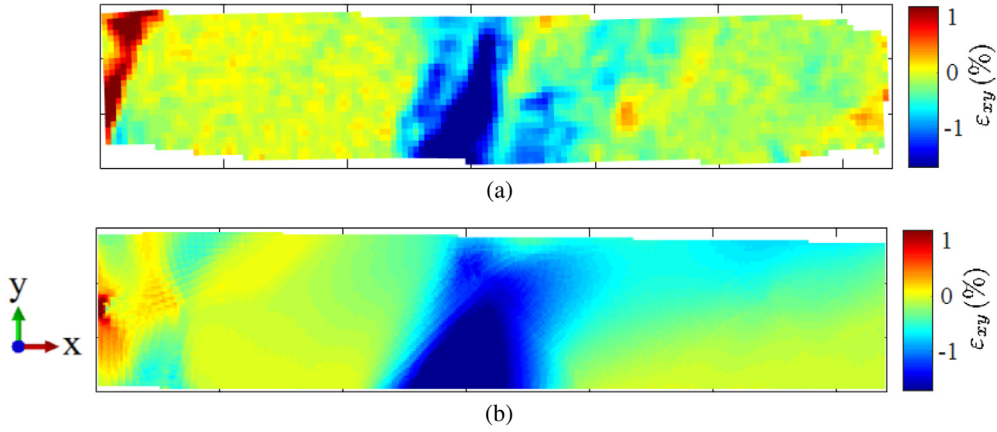
Fig. 12. Shear strain ε_{xy} in the second tensile bar at 1% total strain: (a) DIC measurement, (b) simulation.
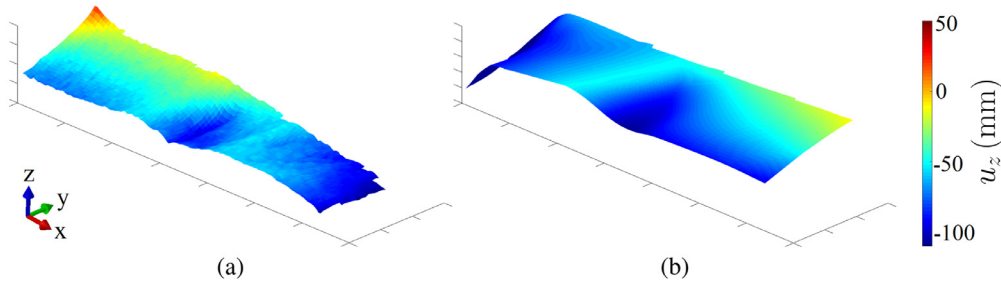

Fig. 13. Out-of-plane displacement u_z in the second tensile bar at 1% total strain: (a) DIC measurement, (b) simulation.

Eight parameters can be extracted because eight different quantities are compared in experiment and simulations: four yield stresses (gauge and individual grains), the maximum stress obtained at 2% strain and the maximum strain reached by each of the grains. The calibration procedure is possible using this particular tensile bar experiment because the four grains show different active deformation mechanisms. As shown in Figs. 6 and 7, grain 1 shows a strong activity of the "wall" slip system, followed by grains 2 and 3. Grain 1 also shows moderate activity of the $(130)[3\bar{1}0]$ twin system, which allows the twin-slip interaction coefficient to be determined. Grain 4 shows strong activity of the $(130)[3\bar{1}0]$ twin system, but also moderate activity of the "floor" slip system, allowing the twin-slip interaction coefficient to be found.

The stress-strain curves in Fig. 5(a)–(c) show that the {130} twin system has a significant strain hardening response. For instance, the yield strength of grain 4 in the first tensile bar increases as the bar is loaded even though most plastic deformation in that grain is provided by a single twin variant $(130)[3\bar{1}0]$, as shown in Figs. 6 and 7. Early studies on twin initiation and growth assumed a constant CRSS for twinning (Christian and Mahajan, 1995). Recent experimental studies (Patriarca et al., 2013) and molecular dynamics simulations (Ojha et al., 2014), however, show that both slip activity and twins affect the CRSS for twinning. This is consistent with the present work, in which the optimisation algorithm automatically identifies the extent of the twin-slip interaction and the interaction between coplanar twins. The comparison between the twin-slip model and twin-coplanar hardening models, reported in Section 2.2, shows that both models can describe the mechanical behaviour of the first tensile bar. It is likely that the twin variant $(130)[3\bar{1}0]$ interacts with both slip systems and coplanar twins. The present approach is not able to distinguish between these two interactions, but it can provide values for the interaction coefficients k_β^1.

The determination of the coefficients k_β^1 was not possible in previous works on fine-grained α-uranium, based on tensile and compression tests of textured samples (McCabe et al., 2010), and on neutron diffraction (Brown et al., 2009). This is because these measurements include information from thousands of grains and are not able to discriminate between the slip-slip and slip-twin interactions. Therefore, the interaction coefficients between the slip systems and the {130} twin system were set to zero (see Table 2 in (McCabe et al., 2010)).

Values for the twin hardening coefficients k_β^1 of α-uranium are not available in the literature, but a quantitative comparison with other materials can be made. (Abdolvand and Daymond, 2013b) used a Voce hardening law to describe Zircaloy, in which the CRSS for tensile twins was given in the small strain approximation:

$$\tau_\beta^c \approx \tau_\beta^0 + \theta_\beta^0 \Gamma \tag{17}$$

where Γ is the accumulated shear on all slip/twin systems and $\theta_\beta^0 = 50$ MPa. Assuming that the {130} twin system is the only plastic deformation mechanism, Eq. (12) for the twin-coplanar hardening model becomes:

$$\tau_\beta^c = \tau_\beta^0 + \left(\frac{k_\beta^1 \mu_\beta}{\gamma_\beta^{\text{twin}}}\right)\Gamma \approx \tau_\beta^0 + 323\Gamma \tag{18}$$

where the stress is expressed in MPa. This shows that the values obtained for k_β^1 have the same order of magnitude as in other materials. Generally, the hardening rate found in the present experiments is lower than that found for fine-grained α-uranium. For instance, the dislocation multiplication prefactor of the "wall" slip system reported by McCabe et al. (2010) is $k_1^1/b_1 = 200$ μm^{-1} while the present optimisation algorithm finds a maximum value of $k_1^1/b_1 = 43$ μm^{-1}, as reported in Tables 3 and 4. This is consistent with the finding that the average dislocation density grows faster in fine-grained materials (De Sansal et al., 2010; Haouala et al., 2018).

Mesoscale models for FeCr single crystals, based on molecular dynamics simulations (Ojha et al., 2014), show that the twin migration stress grows linearly with the residual Burgers vector left at the twin interface during twin-dislocation interaction (see figure 14 in (Ojha et al., 2014)). Those simulations are carried out in a single crystal with a characteristic dimension of $500w$, where w is the dislocation core width. A migration stress of 167 MPa is found if the residual Burgers vector is $|b_r| = a$, where $a = 0.286$ nm is the lattice constant (Ojha, 2013). Assuming $w \approx a$, the residual Burgers vector in those simulations corresponds to a dislocation density $\rho \approx 1/(500a)^2 \approx 49$ μm^{-2}. The linear relationship between the dislocation density and the twin migration stress gives an increase of 167 MPa / 49 μm^{-2} $\approx$ 3.4 MPa / μm^{-2}. Also Eq. (9) predicts an increase of the CRSS τ_β^c, above which twin volume fraction grows, that depends linearly on the dislocation density; the factor of proportionality is $k_\beta^1 \mu_\beta b_\beta b_\alpha \approx 14$ MPa / μm^{-2}. This comparison shows the consistency between the present model, calibrated without imaging individual twins, and atomistic models, which determine the interaction between dislocations and twins at the sub-micron length scale.

The uncertainty in the present optimisation procedure arises from the approximation that the four grains of the first tensile bar in Fig. 1 each have uniform crystal orientations. An uncertainty quantification procedure was carried out: the Euler angles representing the crystal orientation were sampled at different points in the 4 grains; for instance, this leads to an uncertainty of about 20% on the Schmid factor of the "wall" slip system. The optimisation procedure has been repeated with different Euler angles. The uncertainty is small, about 2%, on the constant friction stress τ_1^0 and on the dislocation multiplication prefactor k_1^1 of the "wall" slip system, and it is about 30% for τ_β^0 and k_β^1 of the twin system.

The constant friction stress of the "chimney" slip system has a large uncertainty: if the value is changed, the residual R_{CRSS} of the optimisation procedure does not change significantly. This is because of the low Schmid factor of the "chimney" slip system in the 4 grains and the higher CRSS at room temperature. Therefore, the "chimney" slip system is not highly active in the 4 grains.

Neglecting dislocation fluxes and dislocation propagation through grain boundaries is reasonable as the grain clusters analysed have a characteristic size of several millimetres. Strain gradient terms in the model are not expected to have a large effect on the stress-strain curves of these individual grains. The CRSS parameters found using the calibration procedure give information about the Hall-Petch effect for slip and twin systems in α-uranium because the calibrated parameters in Table 4 can be compared with the parameters for fine-grained α-uranium (McCabe et al., 2010) and the parameters for single crystals (Daniel et al., 1971).

6. Conclusions

An optimisation procedure was developed to find the slip-twin interaction mechanisms and the parameters of a dislocation-based constitutive model, implemented in a crystal plasticity finite element framework. DIC measurements were made during tensile tests on coarse-grained α-uranium bars containing a small number of grains. This allows us to find the average strain in a grain and to plot the stress-strain curves of individual grains, which can be directly compared to the simulations.

The constitutive model includes the activity of 8 slip systems and 2 twin variants, as previously identified in α-uranium (Zhou et al., 2016). Three different models for the hardening of the twin systems were compared. Models which account for the interaction between twin and slip systems and the interaction between coplanar twins can explain the experimental data. The optimisation procedure is able to find the values of the interaction coefficients, which have not been identified in previous studies on α-uranium.

The optimisation procedure is based on consideration of the average response of the grains within the coarse-grained specimen. The resulting model has been validated by comparing the detailed experimental and simulated strain and displacement fields within the same specimen and for a second tensile specimen with a different grain structure. These are interpreted by analysing the activity of twin/slip systems and the direction of their Burgers vectors.

The method presented can be applied to find the CRSS and hardening properties of plastic deformation mechanisms of other coarse-grained materials. The choice of columnar grains aligned along the load axis is crucial and the number of grains needed is related to the number of unknown model parameters. The method has the advantage that the preparation of single crystal samples is not required and a large number of parameters can be determined from a single test.

Declaration of Competing Interest

The authors declare no conflict of interest.

Acknowledgements

Supplementary material

Supplementary material associated with this article can be found, in the online version, at doi:10.1016/j.jmps.2019.103800

References

Abdolvand, H., Daymond, M.R., 2013a. Multi-scale modeling and experimental study of twin inception and propagation in hexagonal close-packed materials using a crystal plasticity finite element approach; part i: average behavior. J. Mech. Phys. Solids 61 (3), 783–802. doi:10.1016/j.jmps.2012.10.013.

Abdolvand, H., Daymond, M.R., 2013b. Multi-scale modeling and experimental study of twin inception and propagation in hexagonal close-packed materials using a crystal plasticity finite element approach; part ii: local behavior. J. Mech. Phys. Solids 61 (3), 803–818. doi:10.1016/j.jmps.2012.10.017.

Arsenlis, A., Parks, D.M., 2002. Modeling the evolution of crystallographic dislocation density in crystal plasticity. J. Mech. Phys. Solids 50 (9), 1979–2009. doi:10.1016/S0022-5096(01)00134-X.

Asaro, R., 1983. Crystal plasticity. J. Appl. Mech. 50 (4b), 921–934. doi:10.1115/1.3167205.

Asaro, R., Needleman, A., 1985. Overview no. 42 texture development and strain hardening in rate dependent polycrystals. Acta Metall. 33 (6), 923–953. doi:10.1016/0001-6160(85)90188-9.

Bachmann, F., Hielscher, R., Schaeben, H., 2011. Grain detection from 2d and 3d EBSD data-Specification of the MTEX algorithm. Ultramicroscopy 111 (12), 1720–1733. doi:10.1016/j.ultramic.2011.08.002.

Beeler, B., Deo, C., Baskes, M., Okuniewski, M., 2013. First principles calculations of the structure and elastic constants of α, β and γ uranium. J. Nucl. Mater. 433 (1), 143–151. doi:10.1016/j.jnucmat.2012.09.019.

Behmer, G., 2018. Discrete Dislocation Modelling of Uranium. University of Oxford Master's Thesis.

Belytschko, T., Liu, K., Moran, B., Elkhodary, K., 2014. Nonlinear Finite Element Analysis for Continua and Structures, 2nd ed. John Wiley & Sons, New York.

Beyerlein, I., Tomé, C., 2008. A dislocation-based constitutive law for pure Zr including temperature effects. Int. J. Plast. 24 (5), 867–895. doi:10.1016/j.ijplas.2007.07.017.

Brown, D., Bourke, M., Clausen, B., Korzekwa, D., Korzekwa, R., McCabe, R., Sisneros, T., Teter, D., 2009. Temperature and direction dependence of internal strain and texture evolution during deformation of uranium. Mater. Sci. Eng. 512 (1), 67–75. doi:10.1016/j.msea.2009.02.004.

Cahn, R., 1953. Plastic deformation of alpha-uranium; twinning and slip. Acta Metall. 1 (1), 49–70. doi:10.1016/0001-6160(53)90009-1.

Cahn, R.W., 1951. Twinning and slip in α-uranium. Acta Crystallogr. 4 (5), 470. doi:10.1107/S0365110X51001483.

Calhoun, C., 2016. Thermomechanical response of polycrystalline α-uranium. University of Virginia PhD Thesis.

Calhoun, C., Garlea, E., Sisneros, T., Agnew, S., 2015. Effects of hydrogen on the mechanical response of α-uranium. J. Nucl. Mater. 465, 737–745. doi:10.1016/j.jnucmat.2015.07.008.

Calhoun, C., Garlea, E., Sisneros, T., Agnew, S., 2018. In-situ neutron diffraction characterization of temperature dependence deformation in α-uranium. J. Nucl. Mater. 502, 60–67. doi:10.1016/j.jnucmat.2018.01.036.

Calhoun, C., Wollmershauser, J., Brown, D., Mulay, R., Garlea, E., Agnew, S., 2013. Thermal residual strains in depleted α-u. Scr. Mater. 69 (8), 566–569. doi:10.1016/j.scriptamat.2013.06.004.

Capolungo, L., Beyerlein, I., Kaschner, G., Tomé, C., 2009. On the interaction between slip dislocations and twins in hcp zr. Mater. Sci. Eng. 513–514, 42–51. doi:10.1016/j.msea.2009.01.035.

Chen, D., Li, R., Lang, D., Wang, Z., Su, B., Zhang, X., Meng, D., 2017. Determination of the mechanical properties of inclusions and matrices in α-u and aged U-5.5Nb alloy by nanoindentation measurements. Mater. Res. Express 4 (11), 116516. doi:10.1088/2053-1591/aa9864.

Christian, J., Mahajan, S., 1995. Deformation twinning. Prog. Mater. Sci. 39 (1), 1–157. doi:10.1016/0079-6425(94)00007-7.

Clausmeyer, T., Boogaard, T.v.d., Noman, M., Gershteyn, G., Scharper, M., Svendsen, B., Bargmann, S., 2011. Phenomenological modeling of anisotropy induced by evolution of the dislocation structure on the macroscopic and microscopic scale. Int. J. Mater. Form. 4 (2), 141–154. doi:10.1007/s12289-010-1017-4.

Daniel, J., Lesage, B., Lacombe, P., 1971. The influence of temperature on slip and twinning in uranium. Acta Metall. 19 (2), 163–173. doi:10.1016/0001-6160(71)90128-3.

De Sansal, C., Devincre, B., Kubin, L., 2010. Grain size strengthening in microcrystalline copper: a three-dimensional dislocation dynamics simulation. Key Eng. Mater. 423, 25–32. https://www.scientific.net/KEM.423.25 Cited By 11

Devincre, B., Hoc, T., Kubin, L., 2008. Dislocation mean free paths and strain hardening of crystals. Science 320 (5884), 1745–1748. doi:10.1126/science.1156101.

Dunne, F., Petrinic, N., 2006. Introduction to Computational Plasticity. Oxford university press.

Dunne, F., Rugg, D., Walker, A., 2007. Lengthscale-dependent, elastically anisotropic, physically-based hcp crystal plasticity: application to cold-dwell fatigue in ti alloys. Int. J. Plast. 23 (6), 1061–1083. doi:10.1016/j.ijplas.2006.10.013.

Earp, P., Kabra, S., Askew, J., Marrow, T.J., 2018. Lattice strain and texture development in coarse-grained uranium - a neutron diffraction study. J. Phys. Conf. Ser. 1106 (1), 012012.

Erinosho, T., Cocks, A.C.F., Dunne, F., 2013. Texture, hardening and non-proportionality of strain in bcc polycrystal deformation. Int. J. Plast. 50, 170–192. doi:10.1016/j.ijplas.2013.04.008.

Fisher, E.S., McSkimin, H.J., 1958. Adiabatic elastic moduli of single crystal alpha uranium. J. Appl. Phys. 29 (10), 1473–1484. doi:10.1063/1.1722972.

Franciosi, P., Berveiller, M., Zaoui, A., 1979. Latent Hardening in Fcc Crystals. In: Haasen, P., Gerold, V., Kostorz, G. (Eds.), Strength of Metals and Alloys. Pergamon, pp. 23–28. doi:10.1016/B978-1-4832-8412-5.50012-6.

Garlea, E., Bridges, R., Garlea, V., Carpenter, D., Hemphill, M., Morrell, J., 2013. Characterization of a grain size refinement process in cast uranium. Mater. Sci. Eng. 559, 210–216. doi:10.1016/j.msea.2012.08.082.

Grilli, N., Cocks, A.C.F., Tarleton, E., 2019. Crystal plasticity finite element simulations of cast α-uranium. In: Onate, E., Owen, D., Peric, D., Chiumenti, M. (Eds.), Computational plasticity XV: fundamentals and applications. 15th International Conference on Computational Plasticity - Fundamentals and Applications (COMPLAS), Barcelona, Spain, Sep 03–05, 2019

Grilli, N., Cocks, A.C.F., Tarleton, E., 2020. Crystal plasticity finite element modelling of coarse-grained α-uranium. Comput. Mater. Sci. 171, 109276. doi:10.1016/j.commatsci.2019.109276.

Grilli, N., Janssens, K., Nellessen, J., Sandlöbes, S., Raabe, D., 2018. Multiple slip dislocation patterning in a dislocation-based crystal plasticity finite element method. Int. J. Plast. 100, 104–121. doi:10.1016/j.ijplas.2017.09.015.

Grilli, N., Janssens, K.G., Swygenhoven, H.V., 2015. Crystal plasticity finite element modelling of low cycle fatigue in fcc metals. J. Mech. Phys. Solids 84, 424–435. doi:10.1016/j.jmps.2015.08.007.

Guan, Y., Chen, B., Zou, J., Britton, T.B., Jiang, J., Dunne, F.P., 2017. Crystal plasticity modelling and hr-dic measurement of slip activation and strain localization in single and oligo-crystal ni alloys under fatigue. Int. J. Plast. 88, 70–88. doi:10.1016/j.ijplas.2016.10.001.

Haouala, S., Segurado, J., LLorca, J., 2018. An analysis of the influence of grain size on the strength of fcc polycrystals by means of computational homogenization. Acta Mater. 148, 72–85. doi:10.1016/j.actamat.2018.01.024.

Ho, J., 2012. Effect of Twinning on Texture Evolution of Depleted Uranium Using a Viscoplastic Self-Consistent Model. Georgia Tech Ph.D. thesis.

Huddart, J., Harding, J., Bleasdale, P., 1980. The effect of strain rate on the tensile flow and fracture of α-uranium. J. Nucl. Mater. 89 (2), 316–330. doi:10.1016/0022-3115(80)90063-X.

Hutchinson, J.W., Hill, R., 1970. Elastic-plastic behaviour of polycrystalline metals and composites. Proc. R. Soc. Lond.. A. Math. Phys. Sci. 319 (1537), 247–272. doi:10.1098/rspa.1970.0177.

Inouye, H., Schaffhauser, S., 1969. Low-temperature ductility and hydrogen embrittlement of uranium - a literature review. ORNL-TM-2563.

Irastorza-Landa, A., Grilli, N., Swygenhoven, H.V., 2017a. Effect of pre-existing immobile dislocations on the evolution of geometrically necessary dislocations during fatigue. Modell. Simul. Mater. Sci. Eng. 25 (5), 055010. doi:10.1088/1361-651x/aa6e24.

Irastorza-Landa, A., Grilli, N., Swygenhoven, H.V., 2017b. Laue micro-diffraction and crystal plasticity finite element simulations to reveal a vein structure in fatigued cu. J. Mech. Phys. Solids 104, 157–171. doi:10.1016/j.jmps.2017.04.010.

Irastorza-Landa, A., Swygenhoven, H.V., Petegem, S.V., Grilli, N., Bollhalder, A., Brandstetter, S., Grolimund, D., 2016. Following dislocation patterning during fatigue. Acta Mater. 112, 184–193. doi:10.1016/j.actamat.2016.04.011.

Jacob, C.W., Warren, B.E., 1937. The crystalline structure of uranium. J. Am. Chem. Soc. 59 (12), 2588–2591. doi:10.1021/ja01291a035.

Jones, E., Oliphant, T., Peterson, P., et al., 2001. SciPy: Open source scientific tools for Python.

Kalidindi, S.R., 1998. Incorporation of deformation twinning in crystal plasticity models. J. Mech. Phys. Solids 46 (2), 267–290. doi:10.1016/S0022-5096(97)00051-3.

Kalidindi, S.R., 2001. Modeling anisotropic strain hardening and deformation textures in low stacking fault energy fcc metals. Int. J. Plast. 17 (6), 837–860. doi:10.1016/S0749-6419(00)00071-1.

Kapoor, R., Behera, A., Chakravartty, J., Hussain, M., 2015. Hot deformation of uranium in the α, β, and γ phases. Metall. Mat. Trans. A 46, 251–259. doi:10.1007/s11661-014-2624-3.

Khan, A., Marrow, T., 2009. In-situ observation of damage mechanisms by digital image correlation during tension and low cycle fatigue of magnesium alloys. In: 12th International Conference on Fracture 2009, ICF-12, 2, pp. 871–879.

Knezevic, M., Capolungo, L., Tomé, C.N., Lebensohn, R.A., Alexander, D.J., Mihaila, B., McCabe, R.J., 2012. Anisotropic stress strain response and microstructure evolution of textured α-uranium. Acta Mater. 60 (2), 702–715. doi:10.1016/j.actamat.2011.10.041.

Knezevic, M., Crapps, J., Beyerlein, I.J., Coughlin, D.R., Clarke, K.D., McCabe, R.J., 2016. Anisotropic modeling of structural components using embedded crystal plasticity constructive laws within finite elements. Int. J. Mech. Sci. 105, 227–238. doi:10.1016/j.ijmecsci.2015.11.021.

Knezevic, M., McCabe, R.J., Lebensohn, R.A., Tomé, C.N., Liu, C., Lovato, M.L., Mihaila, B., 2013a. Integration of self-consistent polycrystal plasticity with dislocation density based hardening laws within an implicit finite element framework: application to low-symmetry metals. J. Mech. Phys. Solids 61 (10), 2034–2046. doi:10.1016/j.jmps.2013.05.005.

Knezevic, M., McCabe, R.J., Tomé, C.N., Lebensohn, R.A., Chen, S.R., Cady, C.M., III, G.T.G., Mihaila, B., 2013b. Modeling mechanical response and texture evolution of α-uranium as a function of strain rate and temperature using polycrystal plasticity. Int. J. Plast. 43, 70–84. doi:10.1016/j.ijplas.2012.10.011.

Lander, G., Fisher, E., Bader, S., 1994. The solid-state properties of uranium. a historical perspective and review. Adv. Phys. 43 (1), 1–111. doi:10.1080/00018739400101465.

Lebensohn, R., Tomé, C., 1993. A self-consistent anisotropic approach for the simulation of plastic deformation and texture development of polycrystals: application to zirconium alloys. Acta Metall. Mater. 41 (9), 2611–2624. doi:10.1016/0956-7151(93)90130-K.

Lim, H., Carroll, J., Battaile, C., Buchheit, T., Boyce, B., Weinberger, C., 2014. Grain-scale experimental validation of crystal plasticity finite element simulations of tantalum oligocrystals. Int. J. Plast. 60, 1–18. doi:10.1016/j.ijplas.2014.05.004.

Lloyd, L.T., Barrett, C., 1966. Thermal expansion of alpha uranium. J. Nucl. Mater. 18 (1), 55–59. doi:10.1016/0022-3115(66)90095-X.

Lukesh, J.S., 1949. Note on the structure of uranium. Acta Crystallogr. 2 (6), 420. doi:10.1107/S0365110X49001107.

Madec, R., Devincre, B., Kubin, L.P., 2002. From dislocation junctions to forest hardening. Phys. Rev. Lett. 89, 255508. doi:10.1103/PhysRevLett.89.255508.

McCabe, R., Capolungo, L., Marshall, P., Cady, C., Tomé, C., 2010. Deformation of wrought uranium: experiments and modeling. Acta Mater. 58 (16), 5447–5459. doi:10.1016/j.actamat.2010.06.021.

Mecking, H., Kocks, U., 1981. Kinetics of flow and strain-hardening. Acta Metall. 29 (11), 1865–1875. doi:10.1016/0001-6160(81)90112-7. Cited By 1384

Nelder, J.A., Mead, R., 1965. A simplex method for function minimization. Comput. J. 7 (4), 308–313. doi:10.1093/comjnl/7.4.308.

Nellessen, J., Sandlöbes, S., Raabe, D., 2015. Effects of strain amplitude, cycle number and orientation on low cycle fatigue microstructures in austenitic stainless steel studied by electron channelling contrast imaging. Acta Mater. 87, 86–99. doi:10.1016/j.actamat.2014.12.024.

Ojha, A., 2013. Modeling of twinning as a deformation mechanism in iron (bcc) crystals and iron-based alloys. University of Illinois at Urbana-Champaign Ph.D. thesis.

Ojha, A., Sehitoglu, H., Patriarca, L., Maier, H., 2014. Twin migration in fe-based bcc crystals: theory and experiments. Philos. Mag. 94 (16), 1816–1840. doi:10.1080/14786435.2014.898123.

Patriarca, L., Abuzaid, W., Sehitoglu, H., Maier, H.J., Chumlyakov, Y., 2013. Twin nucleation and migration in FeCr single crystals. Mater Charact. 75, 165–175. doi:10.1016/j.matchar.2012.11.001.

Pham, M., Holdsworth, S., Janssens, K., Mazza, E., 2013. Cyclic deformation response of aisi 316l at room temperature: mechanical behaviour, microstructural evolution, physically-based evolutionary constitutive modelling. Int. J. Plast. 47, 143–164. doi:10.1016/j.ijplas.2013.01.017.

Qiao, H., Barnett, M., Wu, P., 2016. Modeling of twin formation, propagation and growth in a mg single crystal based on crystal plasticity finite element method. Int. J. Plast. 86, 70–92. doi:10.1016/j.ijplas.2016.08.002.

Remy, L., 1978. Kinetics of f.c.c. deformation twinning and its relationship to stress-strain behaviour. Acta Metall. 26 (3), 443–451. doi:10.1016/0001-6160(78)90170-0.

Rollett, A., Lowe, T., Follansbee, P., Daehn, G., 1991. Comparison of experimental and theoretical texture development in alpha uranium. In: proceedings of symposium on Modeling the Deformation of Crystalline Solids. Published by TMS (Warrendale), pp. 361–368.

Roters, F., Diehl, M., Shanthraj, P., Eisenlohr, P., Reuber, C., Wong, S., Maiti, T., Ebrahimi, A., Hochrainer, T., Fabritius, H.-O., Nikolov, S., Friák, M., Fujita, N., Grilli, N., Janssens, K., Jia, N., Kok, P., Ma, D., Meier, F., Werner, E., Stricker, M., Weygand, D., Raabe, D., 2018. DAMASK - The düsseldorf advanced material simulation kit for modeling multi-physics crystal plasticity, thermal, and damage phenomena from the single crystal up to the component scale. Comput. Mater. Sci. doi:10.1016/j.commatsci.2018.04.030.

Roters, F., Eisenlohr, P., Hantcherli, L., Tjahjanto, D., Bieler, T., Raabe, D., 2010. Overview of constitutive laws, kinematics, homogenization and multiscale methods in crystal plasticity finite-element modeling: theory, experiments, applications. Acta Mater. 58 (4), 1152–1211. doi:10.1016/j.actamat.2009.10.058.

Roters, F., Eisenlohr, P., Kords, C., Tjahjanto, D., Diehl, M., Raabe, D., 2012. Damask: the düsseldorf advanced material simulation kit for studying crystal plasticity using an fe based or a spectral numerical solver. Procedia IUTAM 3, 3–10. doi:10.1016/j.piutam.2012.03.001. IUTAM Symposium on Linking Scales in Computations: From Microstructure to Macro-scale Properties

Roters, F., Wang, Y., Kuo, J.-C., Raabe, D., 2004. Comparison of single crystal simple shear deformation experiments with crystal plasticity finite element simulations. Adv. Eng. Mater. 6 (8), 653–656. doi:10.1002/adem.200400079.

Shen, B., Paulino, G.H., 2011. Identification of cohesive zone model and elastic parameters of fiber-reinforced cementitious composites using digital image correlation and a hybrid inverse technique. Cem. Concr. Compos. 33 (5), 572–585. doi:10.1016/j.cemconcomp.2011.01.005.

Sutcliffe, J., Petherbridge, J., Cartwright, T., Springell, R., Scott, T., Darnbrough, J., 2018. Preparation and analysis of strain-free uranium surfaces for electron and x-ray diffraction analysis. arXiv e-prints.

Taplin, D., 1967. J. Aust. Inst. Met. 12, 32.

Taplin, D., Martin, J., 1963. The effect of grain shape on the tensile properties of α uranium. J. Nucl. Mater. 10 (2), 134–139. doi:10.1016/0022-3115(63)90078-3.

Yanzhi, Z., Xiaolin, W., Xianglin, C., Dawu, X., 2015. In situ x-ray diffraction study of the tensile deformation of u-5.8nb alloy. Rare Metal Mater. Eng. 44 (5), 1094–1098. doi:10.1016/S1875-5372(15)30073-4.

Zecevic, M., Knezevic, M., Beyerlein, I.J., McCabe, R.J., 2016a. Origin of texture development in orthorhombic uranium. Mater. Sci. Eng. 665, 108–124. doi:10.1016/j.msea.2016.04.018.

Zecevic, M., Knezevic, M., Beyerlein, I.J., McCabe, R.J., 2016b. Texture formation in orthorhombic alpha-uranium under simple compression and rolling to high strains. J. Nucl. Mater. 473, 143–156. doi:10.1016/j.jnucmat.2016.02.021.

Zhou, P., Xiao, D., Wang, W., Sang, G., Zhao, Y., Zou, D., He, L., 2016. Twinning behavior of polycrystalline alpha uranium under quasi static compression. J. Nucl. Mater. 478, 83–90. doi:10.1016/j.jnucmat.2016.05.041.